2D Bifunctional Tungsten Disulfide Embedded with UiO-66 (WS_2@UiO-66) as highly active Electrocatalyst for Overall Water Splitting.

By

Muhabbat Shah

School of Chemical and Materials Engineering

National University of Sciences and Technology

2022

2D Bifunctional Tungsten Disulfide Embedded with UiO-66 (WS_2@UiO-66) as highly active Electrocatalyst for Overall Water Splitting.

Name: Muhabbat Shah

Reg.No:0000320510

This thesis is submitted as a partial fulfillment of the requirements for the degree of

''MS in Chemical Engineering''

Supervisor Name: Dr. Erum Pervaiz

School of Chemical and Materials Engineering (SCME)

National University of Sciences and Technology (NUST)

H-12 Islamabad, Pakistan

June 2022

Dedication

By the mercy of Almighty Allah, the Most Merciful and Most Beneficent, this study is dedicated to my beloved parents who have always provided right direction and support. To my supervisor, who shared her knowledge, provided me guidance, and pushed me to complete my objectives. And to all my coworkers with whom I've enjoyed beautiful memories.

Acknowledgement

There is none other but Almighty Allah, whose will be required for everything and anything in this world, who blessed us with the ability to think and made us willing to explore the entire universe. Infinite greetings to the Holy Prophet Muhammad (PBUH), the cause of the universe's creation and a fountain of knowledge and blessing for all humanity.

Dr. Erum Pervaiz, my renowned supervisor, deserves credit for trusting in my talents. Her constant guidance, encouragement, and support were vital in the project's success. I'd want to articulate my heartfelt thankfulness to my deserving GEC members, Dr. Sara Farrukh, Dr. Tayyaba Noor and Dr. Umair Sikander. The unwavering moral support that my family and friends have always provided will always be my light in the dark. My heartfelt gratitude goes out to all the personnel and lab attendants' Thank you!

Abstract

Effective water splitting by electro catalysts provides greater potential for producing hydrogen fuel in renewable energy devices. To use high-performance water splitting electrocatalysts, an economically stable, viable, and effective electrocatalyst with lower activation potential barriers is usually required. We provide a solvothermal approach to develop of active electrocatalyst (WS_2@UiO-66) catalyst for effective and quick hydrogen evolution process. In general, the WS2/UiO-66 heterostructure allows for an efficient water splitting process. The hydrogen evolution reaction (HER) and the oxygen evolution reaction (OER) may better diffuse and transfer electrons across the heterojunction interface due to the open structure and increased number of active sites of this bifunctional design. A current density of 10 mA/cm2 may be reached in an alkaline solution with the WS_2 @UiO-66 by applying an overpotential of just 121.1 mV for HER and 220 mV for OER. Tafel slope values of 272 mV.dec-1 for the HER and OER catalysts are the best. WS_2@UiO-66 can also sustain HER/OER activity for 24 hours at a current density of 10 mA/cm2.WS_2/outstanding UiO-66 bifunctional catalytic performance can significantly speed up its utilization in overall water splitting. This research might cover the way for new methods to develop and prepare very cost-effective energy storage and conversion catalysts.

Key Words: Electrochemical Water splitting, Tungsten sulfide, UiO-66, Hydrogen Evolution Reaction (HER), Oxygen Evolution Reaction (OER)

Table of Contents

List of Figures

List of Tables

Abbreviations

HER: Hydrogen evolution Reaction

OER: Oxygen evolution Reaction

PEC: Photo-Electrochemical water splitting

ECAS: Electrochemical Active Surface Area

TOF: Turnover frequency

WS_2: Tungsten Sulfide

MOF: Metallic Organic framework

FE: Faradaic Efficiency

OX: Oxidation

Red: Reduction

Dec-1: Deca

E_C: Cathode overpotential

E_A: Anode over potential

E_R: Excessive Over potential

E_{OP}: Total Over potential for water splitting

Chapter 1

Introduction

Because of the rising environmental pollution and energy crises, exploration and advancement of hydrogen energy has become much more urgent[1-3].For its unlimited source from water and zero greenhouse gas emissions, hydrogen is seen as a favorable future energy carrier[4, 5].For its extremely high energy density and caloric values, It is expected to be utilized extensively in both transportation and stationary energy [6, 7]. Water splitting, which is powered from variable renewables such as wind power and solar, may create high purity hydrogen at a low cost[8, 9]. The water splitting process consists of two process Oxygen Evolution Reaction at the anode and Hydrogen Evolution Reaction at the cathode[10, 11] . Noble metal catalysts which are currently the best effective catalysts for the process of water splitting, but as a result of their lack and huge cost, they are not economically viable for large-scale applications [12, 13]. As a substitute to noble-metal catalysts, transition metal sulfides have evolved. Because they are abundant on Earth, the cost of catalysts will be significantly reduced[14, 15].Their poor efficiencies for HER and OER, on the other hand, fall short of the commercial need for water electrolysis. As a result, exploitation of these earth-abundant catalysts with high stability and activity should be given top priority [13, 16, 17].

According to the findings of a recent research, heterostructure electro catalysts are better than single-component catalysts when it comes to the process of water splitting. The lattice deformation and ligand mismatch that occur at the heterojunction contact lead to the formation of exposed edges and defects. [18-20].During the HER or OER processes, these defect midpoints might function as active sites for middle adsorption. Furthermore, the 3D design enables for rapid mass dispersion and greatly lowers overpotential, notably at the high current densities for OER and HER[21, 22]. Recent study has showed that two-dimensional WS_2 based materials might be effective electrocatalysts due to the high thermoneutral GH of transition metal and chalcogenide edges [23-25]. Exfoliation of WS_2 liquid phase nanosheets is widely acknowledged as a

reliable method for producing large yields of active layered LPE (liquid phase exfoliated)-WS_2 nanosheets. The electrocatalysts are greatly aided by LPE-WS_2, which has extensively exposed edges and a low impedance to charge transfer[24].

Tungsten disulfide (WS_2) is another TMDs material that has a similar crystal and electrical structure to MoS_2 and has been the subject of current research due to its high HER activity[26, 27]. Changqi Sun et al. also discovered that increasing the intrinsic conductivity of WS_2 enhanced HER activity in N-doped WS_2 nanosheets. Despite substantial progress, the search for HER catalysts has mostly focused on the development of platinum-free electrocatalysts, ignoring the incorporation of additional driving elements[25].

In this paper, we propose a rational design of WS_2/UiO-66 2D nanostructure for OER and HER catalysis in alkaline conditions. These WS_2@UiO-66 2D nanostructure on Nickel foam, which can minimize WS_2 aggregation, promote mass diffusion, speed electron transport, and provide HER and OER additional active sites. Because of the synergistic effect generated at the heterojunction interface between WS_2 and UiO-66 phase, which can provide rapid charge transit, which may dramatically improve HER and OER performance in alkaline solution. WS_2 film is made up of tiny WS_2 clusters that are built up of smaller WS_2 nanosheets, and this hierarchical film may be employed as a self-supported electrode for HER when combined with a metal substrate. The WS_2 nanosheets' random orientations and small sizes would considerably aid in the exposing of active edge locations. As a result, the WS_2 film electrocatalyst exhibits superior electro catalytic performance, including a low overpotential (121 mV) to reach current density of -10 mA/cm^2, and excellent catalytic durability by performing ultralong HER operations in basic environment at a static over potential (> 24 h).

1.1 The Basics of Water Splitting

In water splitting, the three most common components are a cathode/anode pair, an electrolyte that is mostly composed of water, and an external bias. [28, 29]. During the process of electrochemical water splitting, there are two separate reactions that take place: the anode-based OER and the cathode-based HER (cathode). A simplified representation of a water-splitting system is shown in figure 1. During the electrolysis

process, the surfaces of the cathode and the anode produce gases composed entirely of H2 and O2, respectively. Different mechanisms are used, one of which is determined by the electrolyte.

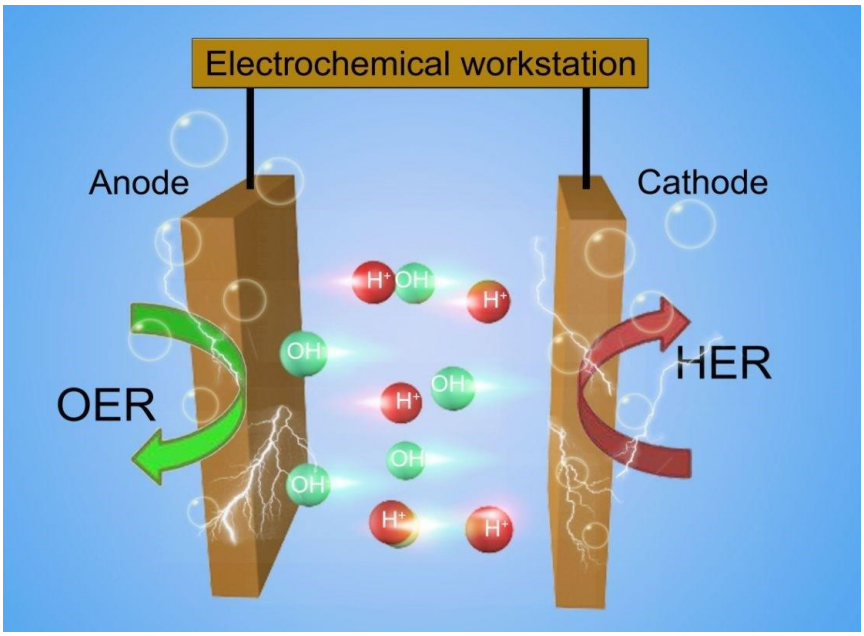

Figure 1: Represents the splitting process of overall water (OER at anode to produced O_2 and HER at cathode produced H_2 via reduction of H^+). Exclusive copy rights 2021 Li, W., et al. [30]

While at acidic electrolyte

HER $4H^+ + 4e^- \longrightarrow 2H_2$ E=0V Eq (1)

OER $2H_2O + 4e^- \longrightarrow O_2 + 4H^+$ E=1.23V Eq (2)

In basic electrolyte

HER $4H_2O + 4e^- \longrightarrow 2H_2 + 4OH^{-1}$ E=0.828V Eq (3)

OER $4OH^{-1} - 4e^- \longrightarrow 2H_2O + O_2$ E=0.402V Eq (4)

Final water splitting reaction

$$2\ H_2O \longrightarrow 2\ H_2 + O_2 \qquad \text{Eq (5)}$$

The potential thermodynamical voltage that is required for the water splitting is 1.23 V at 1 atm and 298 K. Irrespective of whether the electrolyte is alkaline or acidic in nature [31]. Because of this, the voltage that is applied to the water during the electrolysis process must be higher than 1.23 volts. Because of fundamental activation impediment, the excess potential is defined as the overpotential.

$$E_{OP} = E + E_A + E_C + E_R \qquad E = 1.23\ V \qquad \text{Eq (6)}$$

Over potentials for OER and HER are denoted by the symbols EA at the anode and EC at the cathode. Electrolytic diffusion and surface polarization, for instance, may both contribute to the generation of excessive potential. In addition to this, it is essential to take into consideration the possibility of a counter-electromotive force. In order for electro catalysts to be effective against OER and HER, it is necessary for the cathode and anode surfaces to carry out two essential EC and EA activities. By using electro catalysts as cathode or anode materials, it is feasible to reduce EA and EC, and the electro catalytic behavior increases yield on considerable gains.[30].

1.1.1 Hydrogen Evolution Reaction

Hydrogen evolution reaction is done on 2 stages in which two electrons are transfer on the cathode sides. During this electrochemical reaction both the Volmer-Tafel and Volmer-Heyrovsky processes are two distinct routes. As shown in Figure 2 during these 2 stages of cathode side.

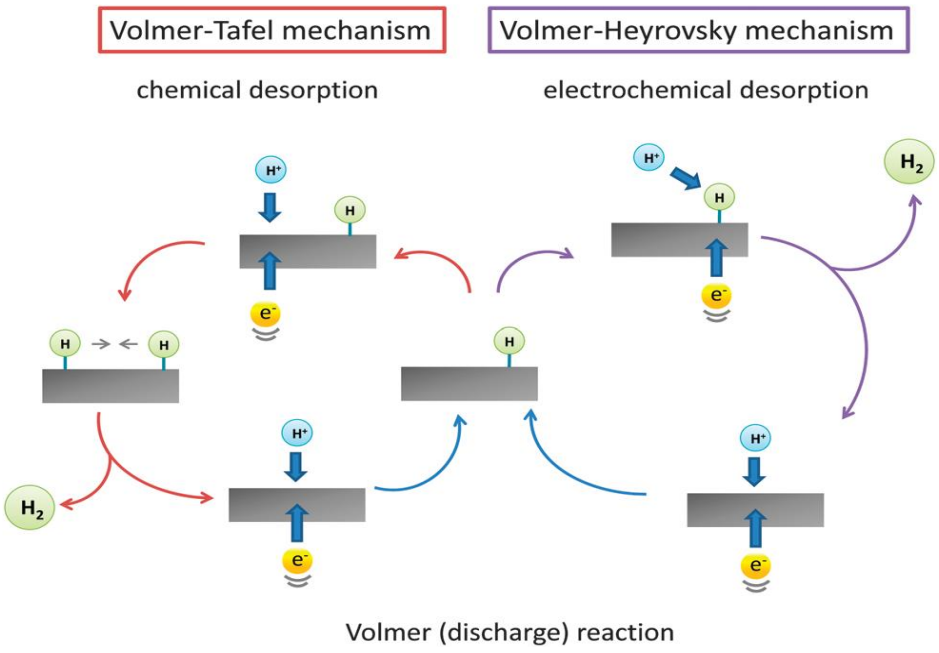

Figure 2 "[(The H2 evolution tool on the apparent of an electrode in acidic liquids. Copy rights 2014 Morales, C.G., and et.al.)]"[32].

The Volmer-Tafel and Volmer-Heyrovsky mechanisms follows desorption phenomena both chemical and electrochemical, respectively. The reactions mentioned below

The Volmer reaction.
Volmer reaction is an electrochemical method that results in hydrogen adsorption. Where proton combines with electron on the surface of catalyst in acidic solution to create the active intermediate H*.

Heyrovsky reaction
Another sort of electrochemical desorption method is the Heyrovsky reaction. H* reacts with the H* and the electrons to produce H2 molecules in an acidic electrolyte.

In acidic solution

$$M\text{-}H^{*} + H^{+} + e^{-} \longrightarrow M + H_2 \qquad \text{Eq (9)}$$

Tafel reaction
The mechanism for the process of chemical desorption happens while two adsorbed molecules of H* are combine at the catalytic surface and to produce H_2.

For the acidic and or the alkaline solution

$$2M\text{-}H^{*} \longrightarrow 2M + H_2 \qquad \text{Eq (10)}$$

1.1.2 Oxygen Evolution Reaction

In comparison to HER on cathode, OER on the anode is a 4-electron mechanism including numerous intermediates. The OER is kinetically sluggish and has a significant overpotential associated to the hydrogen evolution process owing to the multiple step mechanism and energy required (HER). Furthermore, because it functions differently in acidic and basic media, OER is highly dependent on the pH of the electrolytic nature solution. Using a 0.404V potential, two H2O molecules are oxidized in acidic. Using 1.230 V, the OH- group is transformed into O2 and H2O in this alkaline medium (vs RHE). From the foregoing, it can be deduced that the mechanism is less active more capably in an acidic environment than in an alkaline one [33, 34].

During OER, the subsequent reactions happen:
At Acidic Electrolyte

$$H_2O + (M) \longrightarrow (M)\text{-}^{*}OH + H^{+} + e^{-} \qquad \text{Eq (11)}$$

$$(M)\text{-}^{*}OH \longrightarrow (M)\text{-}O^{*} + H^{+} + e^{-} \qquad \text{Eq (12)}$$

$$(M)\text{-}O^{*} + H_2O \longrightarrow (M)\text{-}^{*}OOH + H^{+} + e^{-} \qquad \text{Eq (13)}$$

$$(M)\text{-}^{*}OOH \longrightarrow (M) + O_2 + H_2O + e^{-} \qquad \text{Eq (14)}$$

While at Alkaline Electrolyte

$$OH^- + (M) \longrightarrow (M) - {}^{*}OH + e^- \quad \text{Eq (15)}$$

$$(M)-{}^{*}OH + OH^- \longrightarrow (M) - O^{*} + H_2O + e^- \quad \text{Eq (16)}$$

$$(M)-O^{*} + OH^- \longrightarrow (M)-{}^{*}OOH + e^- \quad \text{Eq (17)}$$

$$(M)-{}^{*}OOH + OH^- \longrightarrow (M) + O_2 + H_2O + e^- \quad \text{Eq (18)}$$

Numerous intermediates, for example the *OH, O*, and *OOH, have been reported to be produced throughout the OER phase. [35]. Additionally, an electrocatalyst's electrical structure determines its ability to produce *OOH and adsorb *OH, that consumes a considerable impact on OER effectiveness. [36].

1.2 Overall process for water splitting affecting parameters

1.2.1 Band gap

Because light can only be absorbed by a small band gap, the band gap itself has to be big enough to accept the majority of the light that is being transmitted through it. Band gaps in the PEC water splitting process ranging from 1.6 to 2.2 are adequate for the absorption of the majority of the solar spectrum.[37]. It is very necessary to boost the charge-carrying capacity of catalysts in order to generate effective activity when the catalysts are coupled with functional materials.[38].

1.2.2 Crystallinity

In generally, research have revealed that catalyst activity rises as crystallinity rises. Electron-hole pair recombination is eliminated and electron transport is improved because high crystallization prevents grain boundary development and lattice defects. [39].

1.2.3 Particle Size

The particle size has a big influence on catalytic action, with a general trend toward small particle sizes with a lot of specific surface area. The molecule should be as tiny as possible. Furthermore, the greater the surface area, the greater the amount of reactant adsorption. The reduction in particle size does not result in an increase in electro catalytic activity in a way that can be predicted. The possibility of electrons and holes

recombining increases in proportion to the proximity of the charges to one another. As a result, a particle size that is ideal must be determined [39, 40].

1.3 Evolution Parameters for Overall Water Splitting

Evolution methodologies for the OER, HER, and the total water splitting for efficiency are required to compare various types of electro catalysts. In overall, the most efficient and scalable approaches for estimating the effectiveness of splitting are the (i) activity, (ii) selectivity, and (iii) stability methods.[41].

1.3.1 Activity

To evaluate the performance of a water-splitting catalyst, many evolution parameters can be employed. For the oxygen evolution process and HER systems, the three most important factors to evaluate the kinetic activity of Tafel slope, current rate, and the turnover frequency (TOF). Tafel slop is a critical characteristic in defining a catalyst's behavior. It's a graph that depicts the relationship between the current generated by an electrochemical cell. It illustrates how the response rate and the over potential are related because a lesser overpotential is required to achieve. [42]. In other words, and furthermore active catalyst has a larger current density and a smaller Tafel slope. The ability to achieve a current density of 10 mA/cm2 or more is commonly acknowledged as a key factor in thermodynamic evolution. [43]. Therefore, selecting the correct catalyst with strong electrocatalytic activity reduces activation overpotential significantly. The TOF reveals how many moles of H2 or O2 are created each unit active center in each amount of time, reflecting inherent activity of the catalyst [44-46].

1.3.2 Selectivity

In spite of its significance, the selectivity of water splitting is a metric that is seldom taken into account. Estimating the rate at which water degrades using the faradic efficiency method is the preferred method. Reactants in an external circuit take on a certain portion of the total charge in order to complete the circuit.[47]. The Faradaic efficiency may be used to determine the selectivity of an OER or HER catalyst. How many electrons can be transmitted via the Faradaic efficiency of the catalyst.[45]. Gas

chromatography may be used to measure the Faradaic efficiency of the water splitting process (GC). As a result of using this method, the FE values of several well-known HER catalysts are equal to one hundred percent. The FE of a typical OER catalyst is lower than one hundred percent because to a number of different energy losses.

To calculate the Faradaic efficiency for OER calculations, the following formulae are commonly used:

$$\text{Faradaic efficiency} = I_R N_D / I_D N_R N_{CL} \qquad \text{Eq (20)}$$

1.3.3 Stability

One of two approaches will be used to measure catalyst stability[31, 48]. Chronoamperometry is the first, whereas cyclic voltammetry, or LSV measurement is the second. It is possible to see time-dependent fluctuations in current or potential even when the potential or current density is held constant. The reliability of the findings will be assured if the length of the experiment is more than ten hours. The over potential of LSV curves will normally grow after a given number cycles, and a lower increase of overpotential indicates higher stability.

Chapter 2

Literature Review

2.1 Tungsten Sulfide and their hybrids in electrochemical water splitting.

Transition metal hallucinogenic, particularly WS_2, exhibit high catalytic activity and are extremely stable, making them suitable 2D materials for energy applications.

TMDs have proved to have considerable promise as CO2 reduction and water splitting catalysts in both theoretical and empirical studies. [49]. WS_2, on the other hand, has a low electrical conductivity, which limits charge transfer and electro catalytic activity. [50]. By changing the structure of WS_2, a typical two-dimensional material, to expose more active sites, the catalytic performance can be considerably improved. [51]. The development of composites is one of the many strategies for enhancing electrical conductivity that can be used to overcome the big barrier. [52, 53].

Wang et al. the first time, an innovative strategy was established for developing and producing a NiO/Ni ornamented with WS_2 nano sheet arrangement on carbon cloth ($NiO/Ni/WS_2/CC$) composite. It permits an alkaline electrolytic cell with a current density of 10 mA/cm2 at a 1.42 V overpotential, the lowest of any figure ever reported.

The excellent performance is largely due to the unusual 3-D prearrangement and multiphase interaction between WS_2, NiO, and Ni. [54]. Peng et al. studied that 3D Co9S8/WS2 electrode material configuration, $Co9S8/WS_2$ has been reported as an active electro catalyst for water splitting. In an alkaline medium, electro catalysts with hydrogen-evolving 3-D electrodes may yield current densities of up to 10 mA/cm2 with an over potential of 138 millivolts (mV). This multifunctional electrode may also be used to build a high-performance alkaline water electrolytic cell with a current density of 10 mA/cm2 and a cell voltage of 1.65 V.[55].

A unique $TiO2@WS_2$ hybrid was produced by combining a hydrothermal process that required two steps with selective etching. W2 ultra-thin Tin oxide nanotubes with acid-etched surface areas were used as a substrate for the development of nanosheets, which created various layers with visible active-edges. This was accomplished by using the nanotubes as a support for the growth of the nanosheets.

Pure TiO2 or WS2 needed larger over potentials and onset currents, while the hybrid needed just 10 mA/cm2, which is a significant difference.

Additionally, during the alkaline HER process, enhanced cycle stability was discovered, viewing its potential for future applied application. [56]. Tayebi et al. studied WS2/WO3 was synthesized for photo electrochemical water splitting process. The electro-current density of the produced catalyst was extremely high. When the WS2 nanosheets were deposited, the photocurrent density rose dramatically, especially for the WO3/WS2 electrode, with peaks of about 6.6 mA/cm2 current density at 1.75 V vs. Ag/AgCl. The charge transfer at the photoanode–electrolyte interface is linked to the semi-circle radius in a Nyquist plot, reducing the semi-circle radius in an EIS Nyquist plot revealed that charge transfer from tungsten disulfide nanosheets to W/WO3 substrate was simpler than charge transfer from WS2 nanosheets to WS2/WO3 substrate. [57]. There are more charge carriers, improved charge separation, and charge migration because of this. The nanostructures demonstrated a severalfold increase in photocurrent density 0.15 mA/cm2 at 1.23 V vs. RHE in photoelectrochemical total water splitting compared to the plain sulfides. [58]. Liu et al. created high-quality 1T' phase WS2 nanomaterials and 2H phase WS2 nanostructures using a simple colloid synthesis approach, as illustrated in Figure 3. (a).

The strong connection between a positive charge surfactant and WS2 made 1T'-WS2 very stable after surface treatment, allowing it to stand effectively disseminated in a polar solvent.1T'-WS2 had a low 200 mV overpotential, a small Tafel slope of 50.4 mV/dec, and exceptional stability at 10 mA/cm2, as shown in Figure 3. (g-i).

Table 1 The electrocatalytic activity of WS2 doped with metal components.

Catalysts	Reaction type	Electrolyte	Current density (mA/cm^2)	Overpotential (mV)	Tafel slope (mA/dec)	Ref.
WS_2-Co	HER	0.5M H_2SO_4	10	134	76	[59]
WS_2-Co	OER	1M KOH	10	303	79	[60]
WS_2-Co	HER	0.5M H_2SO_4	10	210	49	[61]
Co-WS	HER	0.5M H_2SO_4	10	330	74	[62]
Ni-WS	HER	0.5M H_2SO_4	10	265	55	[62]
Co-WS_x	HER	0.1M phosphate solution	5	238	78	[63]
WS_2-V	HER	0.5M H_2SO_4	10	148	71	[64]
WS_2-Nb	HER	0.5M H_2SO_4	10	750	167	[65]
$W_{1-x}S@Mo_x$	HER	0.5M H_2SO_4	10	178	68	[66]
$W_{1-x}S@Co_x$	HER	0.5M.H_2SO_4	10	121	67	[67]

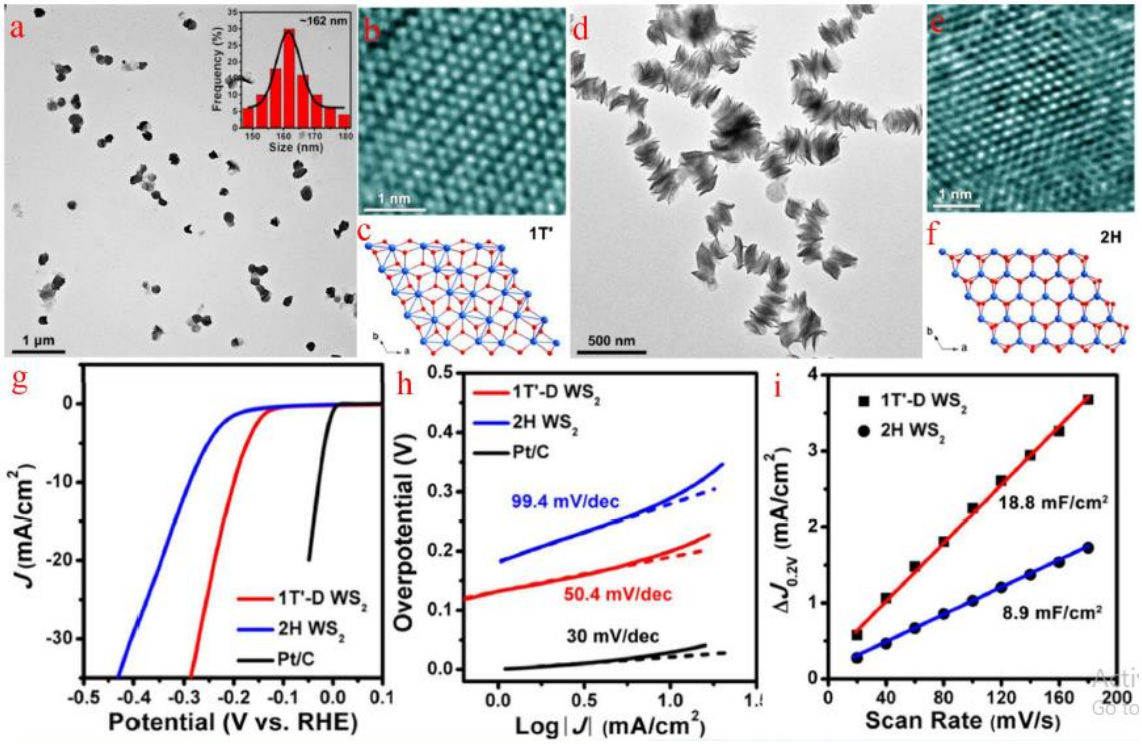

Figure 3: "[(TEM images of WS2 hybrid for (a) NPs and (d) NCs, HRTEM images for WS2 hybrid with (b) NPs and (e) NCs, Atomic structure model for c-axis view of WS2 hybrid with (c) NPs and (f) NCs, (g)LSV OER, (h) TAFEL plot, I Electrochemical surface area at different scan rates.

Doping WS2 with an appropriate metal element is a conventional way for improving its electro catalytic performance. Co-doped WS2 ternary nanosheets were successfully made by Shifa et al the addition of co-loaded tungsten sulphide led to the formation of additional active sites, notably along the highly active S edge. In terms of electro catalytic performance, CoxW (1-x) S2 outperformed pure WS2. A current density of 10 mA/cm2 was recorded at an overpotential current density of 121 mV, and a Tafel slope of 67 mV/dec was detected. [67]. Xu et al. studied that co-doped WS2 was also produced, and the performance of OER was studied. The electrical contact between the Co and S atoms is the reason for this.

When compared to pure WS2, the overpotential property of Co-WS2 was reduced from 492 mV to 303 mV for 10 mA/cm2 current density and displayed decent stability.

The performance of OER was increased by the addition of Co2+ and Co3+ to Co-WS. This led to an increase in OOH* formation and an increase in the capacity to fix

oxygen.[60]. Shi et al. Studied EDS and EELS analyses which shows, 100% of the Co doped was absorbed in to the WS2 lattice utilizing flame vapor depositions in order to create Co-doped W18O49 nanotubes on F.T.O. At the optimal Co doping concentration, the nanotube overpotential dropped by 220 mV, and the Tafel slope dropped from 122/dec to 49 mV/dec at the same current densities.[61].

Table 2 The effectiveness of WS_2 As an electro catalyst by non-metallic elements.

Catalysts	**Type of reaction**	**Electrolyte**	**Current density (mA/cm^2)**	**Overpotential (mV)**	**Tafel slope (mA/dec)**	**Ref.**
WS_2-N	HER	0.5M H_2SO_4	100	197	86	[25]
WS_2-N,P	HER	0.5M H_2SO_4	10	59	35	[69]
WS_2(1-X)Se2x	HER	0.5M H_2SO_4	10	167	107	[70]
WS_2(1-X)Se2x	HER	0.5M H_2SO_4	10	156	69	[71]
WS_2-O	HER	0.5M H_2SO_4	10	-	47	[72]
WS_2(1-X)P_{2X}	HER	0.5M H_2SO_4	10	98	71	[73]
WS_2(1-X)Se2x	HER	0.5M H_2SO_4	10	88	46	[74]
WS_2(1-X)Se2x	HER	0.5M H_2SO_4	10	-	105	[75]

$WS_2@Co_{(1-x)}$,S,N	HER	0.5M H_2SO_4	10	250	64	[76]
$WS_2@Co_{(1-x)}$,S,N	OER	1M KOH	10	365	53	[76]

Water-splitting efficiency can also be improved by using non-metallic metal doping. Maiti et al. The electro catalytic hydrogen production capabilities of exfoliated P and N co-doped WS2 were obtained at the same level as those of pure Pt. When WS2 was co-doped with nitrogen and phosphorus, the end product was mesoporous structures that had many active sites. This made it simpler for HER to form the Volmer and Heyrovsky phases. Enhancements were also made to the electrocatalytic capabilities of on-metal elements such as Se and O. PNEWS2's electrocatalytic activity may be easily seen by referring to Figure 4, where its modest over potential of 59 mV and its moderate Tafel slope of 35 mV/Dec .[25, 70]. Fu et al. developed a method to generate WS2 (1-x) Se2x by first salinizing and then sulfurizing WO3. When added to the crystal structure of tungsten disulfide, selenium has no effect on the structure of the catalyst since its radial radius is far bigger than that of sulphur. An initial 80-volt over potential and an 85-volt/dec rate were observed in the Se2x-WS2 (1-x) monolayer, which was shown to be more effective. This section of the Tafel is known as the Slope. [77].

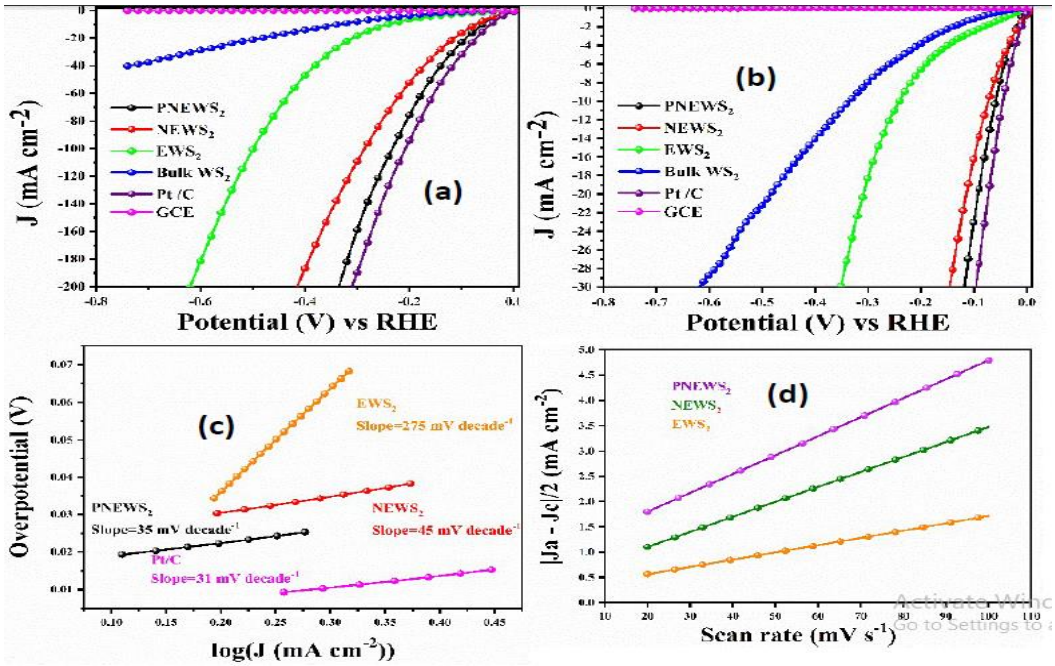

Figure 4: "[((a) At a current density of 200 mv/cm2, performance of catalyst for PNEWS2, NEWS2, EWS2,BULK WS2, Pt/C glassy carbon electrode PNEWS2, NEWS2,EWS2,BULK WS2, Pt/C glassy carbon electrode PNEWS2, NEWS2,EWS2,BULK WS2, Pt/C glassy carbon electrode (b) PNEWS2, NEWS2, EWS2, BULK WS2, Pt/C glassy carbon electrode catalytic performance at current density 30 mv/cm2(c) Tafel plot at 200 mv/cm2 current density(d) Tafel plot at 30 mv/cm2 current density). Exclusive copy rights. Exclusive copy rights 2018 Maiti et.al.)]" [69]

A semi-conducting catalyst is created whenever two or more elements are melted together to form a single substance.[78]. The majority of heterojunctions have precise nanostructures that have been shown to improve electrochemical efficiency. [79, 80].

Table 3 ("[Characteristics activity of the six heterojunction catalysts mentioned were, WS2 hybrids of oxide of metal, hydroxide, noble metal, elemental sulfide, phosphide, and elemental carbon")

Catalysts	Reaction type	Electrolyte	Current density (mA/cm^2)	Overpotential (mV)	Tafel slope (mA/dec)	Ref.
WS_2/Gr-NF	HER	0.5M H_2SO_4	10	185	86	[81]
W_XSCo_y/HCF	HER	0.5M. H_2SO_4	10	228	111	[82]
W_XSCo_y/HCF	HER	0.5M. H_2SO_4	10	437	99	[82]
WS_2/HCF	HER	0.5M H_2SO_4	10	402	288	[82]
WS_2/HCF	OER	0.5M H_2SO_4	10	754	243	[82]
WS_2/SG	HER	0.5M H_2SO_4	10	250	53	[83]
WS_2@W	HER	0.5M H_2SO_4	10	108	46	[84]
WS_2@Si	HER	0.5M H_2SO_4	0.29	99	45	[85]
WS_2/Acetylene black	HER	0.5M H_2SO_4	0.33	-	147	[86]
WS_2@CNTs	OER	0.1M KOH	11	780	62	[87]
WS_2/Carbon/ WS_2	HER	0.5M H_2SO_4	10	175	57	[88]
WS_X/MoS_2	HER	0.5M H_2SO_4	10	213	74	[89]
WS_2@Graphdiyne	HER	0.5M H_2SO_4	10	140	54	[90]

WS_2@N-enriched-carbon foam	HER	0.5M H_2SO_4	10	153	58	[91]
WS_2@Ni_5P_4-Ni_2P	HER	0.5M H_2SO_4	10	94	74	[92]
WS_2@Co-Se_2	HER	0.5M H_2SO_4	10	160	44	[93]
WS_2@Co-S_2	HER	0.5M H_2SO_4	100	245	270	[94]
WS_2@MoS_2 +Bi_2S_4	HER	0.5M H_2SO_4	10	293	-	[95]
WS_2@CdSe	HER	0.5M Na_2SO_4	10	400	56	[96]
WS_2@Pd	HER	0.5M Na_2SO_4	10	130	82	[97]
WS_2@MoS_2	HER	0.5M Na_2SO_4	10	129	72	[98]
WS-Ni	HER	1M KOH	10	38	98	[99]
WS_2@CoS_2	HER	0.5M Na_2SO_4	10	97	66	[100]
WS_2/Ni@NiO	HER	1M. KOH	10	40	83	[54]
WS_2/Ni@NiO	OER	1M. KOH	50	347	108	[54]
WS_2/rGO@WO_3	HER	0.5M.H_2SO_4	10	113	37	[101]
WS_2@Metal hydroxide	HER	1M KOH	10	150	-	[102]
WS_2-Pt@rGO	HER	0.5M H_2SO_4	10	57	47	[103]

WS_2@Pd	HER	0.5M H_2SO_4	10	175	54	[104]
WS_2@Pt	HER	0.5M H_2SO_4	10	80	55	[105]
WS_2@Pt	HER	1M KOH	10	-	27	[106]
WS_2@CoP	HER	0.5M H_2SO_4	10	150	64	[107]

Chapter 3

Material and Methods

3.1 Materials

For the fabrication of all the electrocatalysts, analytical grade chemicals and compounds were utilized (with no processing or purification). Chemicals used include sodium tungstate dihydrate (Na_2WO_4-$2H_2O$), and Sodium sulfide (Na_2S) from Sigma-Aldrich. Merck was a significant contribution to the development of DMF and MMP (NMP). Duksan Pure Chemicals is in the business of producing powdered activated carbon. For the purpose of conducting microbiological analysis, BDH ethanol (C2H5-OH) and deionized water were obtained from a laboratory.

3.2 Preparation of Pure WS_2

The WS_2 NPs electrocatalyst was made using an analytical grade Na_2WO_4-$2H_2O$ and Na_2S in a hydrothermal process with no additional purification. 20 mmol Na_2WO_4-$2H_2O$ and 20 mmol Na_2S were mixed in 50 mL distilled water and agitated constantly for 30 minutes to generate a clear solution in a conventional synthesis. Finally, at 220 °C for 6 hours, the suspension was transferred onto hydrothermal Teflon steel. Centrifugation and ethanol rinsing were used to recover the resultant solution. Finally, the product was collected after being vacuum dried at 70°C.

3.3 Synthesis of WS_2/UiO-66 Hybrids

A one-pot solvothermal synthesis was used to synthesize WS_2 and MOF hybrids at various concentrations. WS_2 and $ZrCl_4$ were added to a solution of 1,4-benzendicarboxylic acid (BDC), dimethylformamide (DMF), and acetic acid in different weight percent ratios (1:1, 1:2, 1:3). For full inclusion of the reactants, the solution was agitated for 30 minutes and then sonicated for 5 hours. The mixtures were heated for 24 hours in a Teflon-lined stainless-steel autoclave at 120°C. The autoclave was cooled to room temperature when the reaction period was completed.

Centrifugation was used to separate the solid product, which was then washed three times with DMF and ethanol. Finally, the product was dried overnight at 70°C.

3.4 Characterization and Electrochemical Study

An X-ray diffractometer was used to perform compositional analyses and phase studies on the developed catalyst (XRD; STOE Germany). The 2θ range for the test was 0°–90°, and Cu-K radiation was used. SEM (JEOL-instrument JSM-6490A) was used to study and investigate the catalyst's structure and morphology, as well as the lattice structure. Brunauer-Emmet-Teller (BET) performed to evaluate surface area and pore size distribution.

Using a three-electrode cell configuration, the electrocatalytic activity was determined under ambient conditions. The electrolyte was a solution of 1.0 M KOH. The counter electrode was composed of Ag/AgCl. The working electrode was constructed of catalyst on Ni-foam, while the counter electrode was built of Pt wire. For calculations following the formula, the potential was changed to a reversible hydrogen electrode (RHE) for standardization equation-1.

$$\mathbf{E_{RHE} = EAg_{/Agcl} + 0.059pH + E^{O}_{Ag/Agcl}} \quad \mathbf{(1)}$$

Where pH= 14

$$\mathbf{E^{O}_{Ag/Agcl} = 0.1976}$$

The performance of electrocatalysts was evaluated using cyclic voltammetry (CV), linear sweep voltammetry (LSV), electrochemical impedance spectroscopy (EIS), and chronopotentiometry. In a potential range of 0 to 1.5 V, linear sweep voltammetry (LSV) was utilized at a scan rate of 10 mV/s. In the potential range of (0–0.6 V), cyclic voltammetry measurements were made at various scan speeds (10, 20, 50, 100, 150) and reported at 50 mV/s. In Tafel plots, overpotential was drawn on the y-axis and log of current density was plotted on the x-axis. The slope was determined by means of a linear equation 2.

$$\dot{\eta} = \mathbf{mlogj + a} \quad \mathbf{(2)}$$

Electrochemical impedance spectroscopy (EIS) has a frequency range of 0.1 Hz to 2 MHz and a 10-mV alternating voltage amplitude. Chronopotentiometry was used to

check the electrocatalyst's stability. The rate of change of potential with constant current (10mA/cm2) is calculated in chronopotentiometry. Stability curves were frequently delivered within 24 hours.

To determine the stability of the produced catalyst, chronopotentiometry tests were performed for 86400s. Electrochemical impedance spectroscopy (EIS) was performed over a frequency range of 200 kHz-100 mHz using an Alternating Current (AC) voltage of 10 mV. The electrochemical active surface area was calculated using. Eq (21)

$$ECSA=C_{ð}/C_s \quad \textbf{(3)}$$

Here $C_{ð}$ shows dual layer capacitance while and Cs shows plain surface identified capacitance per unit area, with a suitable range of 0.040 $mF.cm^{-2}$.

Chapter 4

Results and Discussion

4.1. Characterization of WS_2@UiO-66 based different electrocatalysts

4.1.1. X-ray diffraction analysis

The given Figure 5 shows the XRD pattern of the prepared samples of tungsten disulphide.

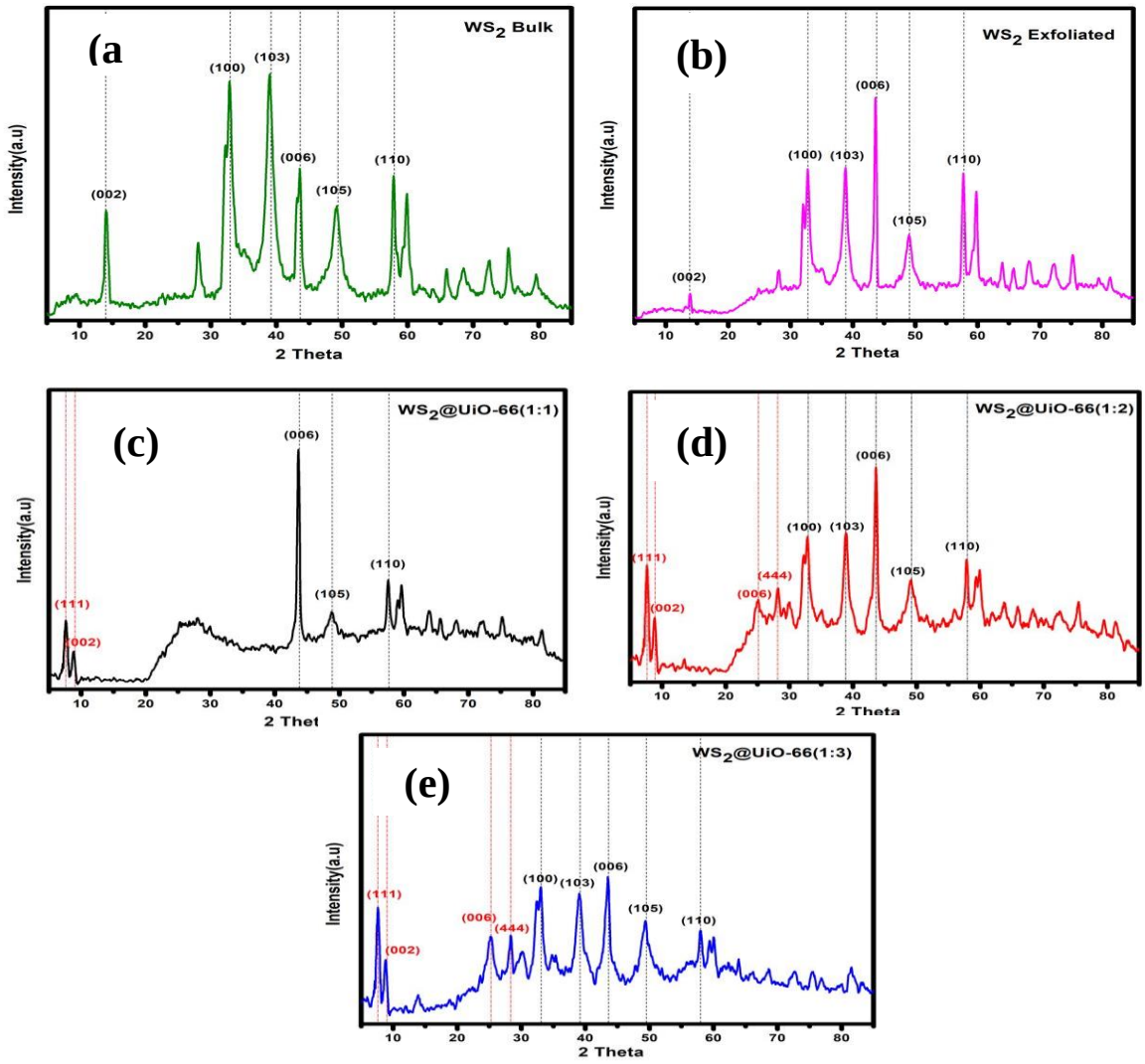

Figure 5 Powder X-ray diffractometry (a) bulk WS2 (b) Exfoliated WS2 (c) WS2@UiO-66 (1:1) (d) WS2 @UiO-66(1:2) (e) WS2 @UiO-66(1:3)

Figure 5 reveals pure and well crystalline peaks of tungsten disulfide nanosheets at 14.36°, 32.76°, 39.59°, 44.05°, 49.79°, and 58.49° analogous to the diffraction planes of (002), (100), (103), (006), (105) and (110), respectively. These patterns are well matched with the XRD patterns of the conventional WS_2 having hexagonal lattice (JCPDS: 84-1398) [108].Other modest diffractions were seen in the (1 0 0), (1 0 3) (105), and (1 1 0) planes. For the hexagonal phase, both diffractions and peak intensities correspond well with the standard JCPDS (JCPDS 08-0237) database[68].UiO-66 was effectively synthesized, as evidenced by the emergence of three distinct peaks position at 2θ = 7.38, 8.56, and 25.67° [109]. Any defect in its crystalline structure is not visible. All the hybrids display the usual UiO-66 peaks, namely those corresponding to the crystallographic planes (111) and (002) at 7.2° and 8.0°, respectively. Moreover crystallites size calculate using Scherrer formula given in equation-3[110].

$D = k\,\lambda/(FWHM)*(Cos\theta)$ (3)

In the above equation FWHM is the integral width (it is basically area under the curve divided by maximal height, taken in radian), D is the apparent size of the crystal and K is a constant whose value is near to 1 (i.e., 0.94), Cu-K 1.54 is the x-ray wavelength, and θ is the Bragg angle.

An average crystal size of 240 Å of bulk tungsten disulfide was calculated using Scherrer calculator, Exfoliated WS_2 is 277 Å, WS_2@UiO-66(1:1) is 244 Å, WS_2@UiO-66(1:2) is 234.5 Å and WS2@UiO-66(1:3) is 179 Å.

4.1.2 Scanning Electron Microscope (SEM)

The microstructures of the synthesized material were determined via SEM examination. Irregular nanosheets of the synthesized WS_2 is produced shown in figure 6(a, b). Based on the SEM morphology of WS_2@UiO-66 (1:1), Nanoparticles without any discernible form might be produced if either structure has just a single kind of shape structure dominating, which is also due to agglomeration. Although certain particles can be observed imbedded in the structure, there is no way to tell them apart. This method of synthesis resulted in a chaotic structure with aggregated particles. UiO-66 structures formed in clusters can be seen in WS_2@Uio-66 (1:2) (Figure-6(d). It's

possible that UiO-66 polyhedral was formed on WS_2 Sheets as a foundation. UiO-66 has a difficult to developing a regular crystalline structure [111]. The morphologies of UiO-66 samples described in the literature have generally composed of uneven intergrown microcrystalline polyhedral shape[7, 112].

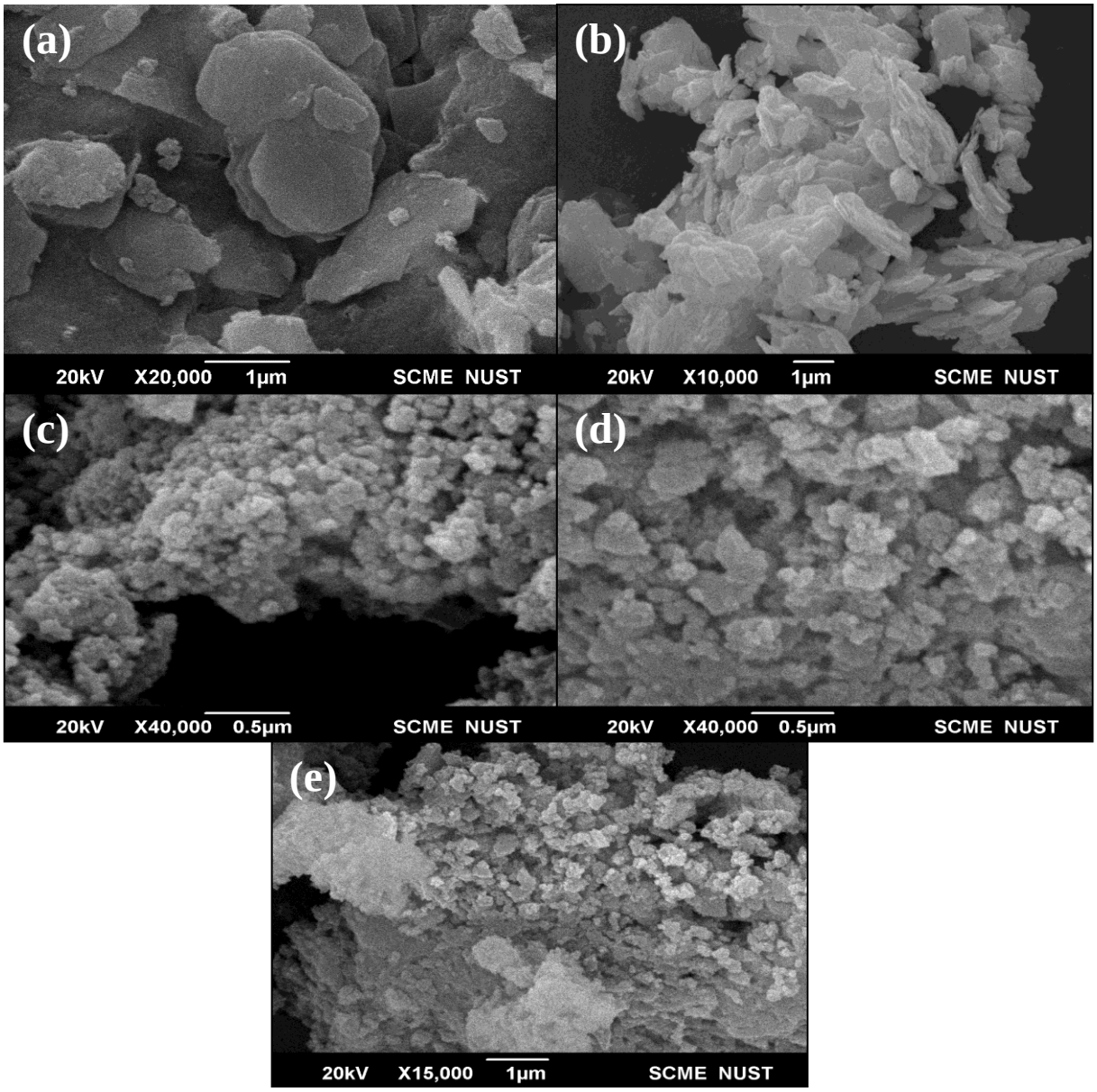

Figure 6 SEM Image of (a) Bulk WS2 (b) Exfoliated WS2 (c) WS2@UiO-66 (1:1) (d) WS2@UiO-66(1:2) (E) WS2@UiO-66(1:3)

4.1.4 BET

Nitrogen adsorption was used to measure the surface area of this type of structure. Using pore size distribution curves and BET analysis many properties can be determined like pore size distribution, pore volume of the hybrid and surface area, as shown in Figure-7(a-b). As by the Brunauer–Deming Teller classification, the isotherm produced for WS_2@UiO-66 (1:2) is of type IV. WS_2@UiO-66(1:2) nanosheets had a pore volume, pore diameter, and surface area of 0.23165 cm^3/g, 4.9 nm, and 125.06 m^2/g, respectively which is very large compared to previous reported WS_2 nanosheets (pore volume is 0.067 cm^3/g, and surface area of 65.05 m^2/g, respectively)[113] . Because prepared materials have a large surface area, the synthesized material might have many active sites on surface and help with electrolyte interaction.

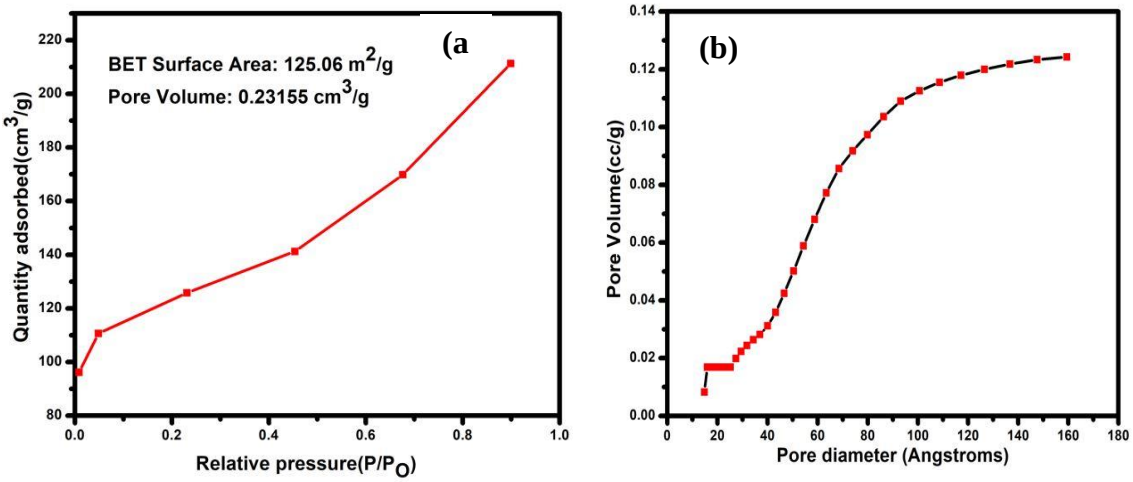

Figure 7 (a) BET adsorption isotherm (b) Pore size distribution curve

4.2 Hydrogen Evolution Reaction (HER)

Figure-8(a) illustrates electrocatalytic HER performance curves for bulk WS_2, Exfoliated WS_2, WS_2@UiO-66 (1:3), WS_2@UiO-66 (1:2), and WS_2@UiO-66 (1:1), as-synthesized catalysts (1:3). Part (a) of Figure-8 shows the linear sweep voltammetry (LSV) charts of all materials. LSV is a metric for electroactive substances' chemical reactivity. WS_2@UiO-66(1:2) demonstrated enhanced HER activity with a small overpotential of 121 mV and the current density of the sample is observed to be 10 mA/cm^2, as seen in the graphs. At the observed current density of 10 mA/cm^2, WS_2 Bulk, Exfoliated WS_2, WS_2@UiO-66 (1:1), and WS_2@UiO-66 (1:3) demonstrated low HER activity with an overpotentials of 149 mV, 153 mV, 123 mV, and 136 mV, respectively. Tafel plots show how the overpotential's response rate is related. Tafel Slope in Figure-4(b) can be used to deduce the response mechanism in the HER.

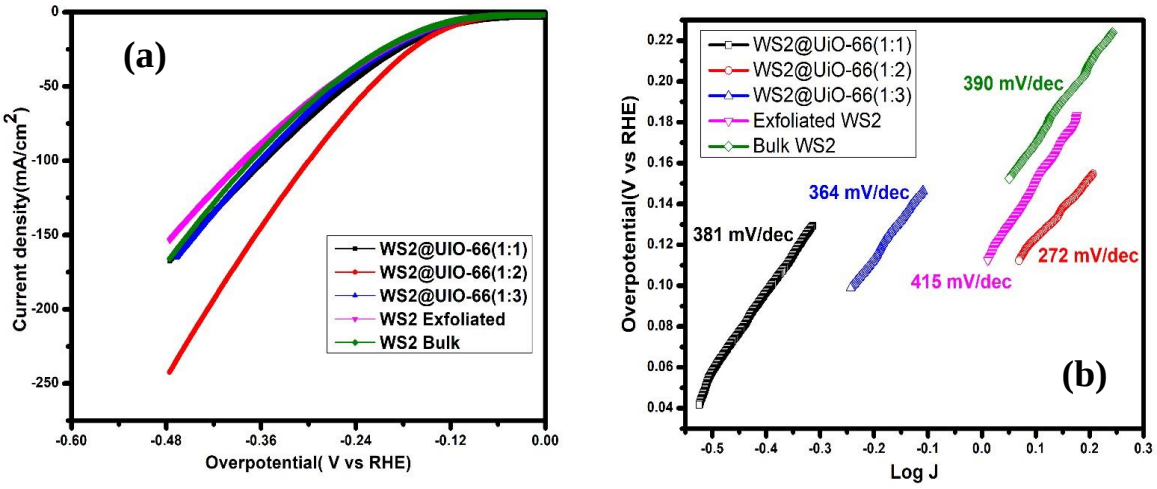

Figure 8 (a) LSV HER curves of Bulk WS2, Exfoliated WS2 , WS2 @UiO-66(1:1, 1:2, 1:3).(b) Corresponding TAFEL plots of Bulk WS2 , Exfoliated. WS2 and WS2 @UiO-66 (1:1, 1:2, 1:3)

The Tafel plot of HER might give the rate-limiting phase. The electron transport is faster in the sample having low Tafel slope, so to achieve high current density and low Tafel slope is needed along with low over potential. Exfoliated WS_2 had the greatest

Tafel slope of 410 mV/dec, whereas WS_2@UiO-66 (1:2) had the lowest with 272 mV/dec, 390 mV/dec, 381 mV/dec, and 364 mV/dec for bulk WS_2, WS_2@UiO-66 (1:1) and WS_2@UiO-66 (1:3) respectively. When the Tafel value is low, hydrogen creation is expedited, and when it is high, it is slowed. The WS2@UiO-66 (1:2) HER exhibits a little decline in performance over the course of 24 hours, but stays constant. It was found that the most effective HER water-splitting catalyst is WS2@UiO-66 (1:2), which is comparable to a number of other highly efficient catalysts (Table-5). There are several factors that contribute to the enhanced performance, including surface area, metal synergy, and the availability of conductive channels in the MOF network

4.3 Oxygen Evolution Reaction (OER)

Figure 9(a) shows LSV polarization curves used to assess OER activity of the prepared electrocatalysts WS_2@UiO-66(1:2) requires an overpotential of round about 220 mV to attain 10 mA/cm^2 current density, which is less than bulk WS_2 (380 mV), Exfoliated WS_2 (403mV), WS_2@UiO-66(1:1) (300mV), WS_2@UiO-66(1:3) (330mV). Figure-9(b) shows a Tafel diagram of the OER reaction kinetics. In compared to bulk WS_2 (185 mV/dec), Exfoliated WS_2 (445 mV/dec), , WS_2@UiO-66(1:1) (355 mV/dec), WS_2@UiO-66(1:3) (320 mV/dec) and WS_2@UiO-66(1:2) (140 mV/dec), WS_2@UiO-66(1:2) exhibits the shortest Tafel slope 140 mV/dec. WS_2@UiO-66(1:2), It offers the highest production for HER as well as OER electrocatalytic water-splitting and is comparable to several highly effective catalysts previously reported (Table-5). The higher surface area as well as the efficient electron transport networks with the appearance of conducting passageways supplied by the MOF network are responsible for the enhanced performance. Due to synergistic effects, bimetallic catalysts typically outperform single metal component catalysts in the water oxidation process, with structural and dependent on composition enhancements of active sites and the capacity to increase the current over potential and current density characteristics. An open structure and bimetallic synergy enable rapid mass movement and enhance electron transmission because a greater number of accessible catalytic sites are easily available. [114].

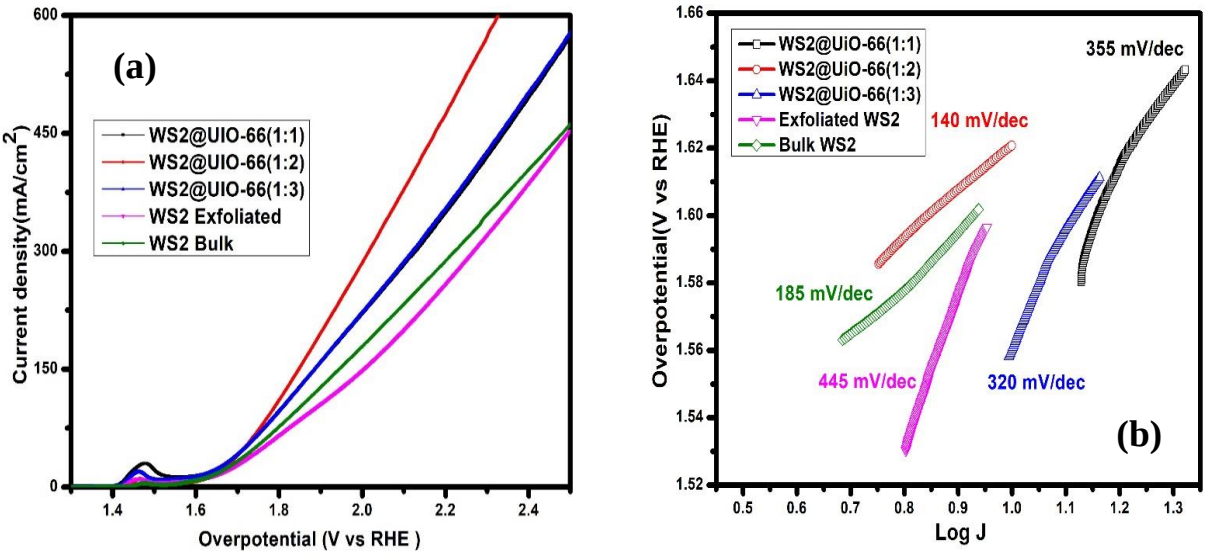

Figure 9 (a) LSV OER curves of Bulk WS2 , Exfoliated WS2, WS2 @UiO-66(1:1, 1:2, 1:3).(b) Corresponding TAFEL plots of Bulk WS2, Exfoliated WS2 and WS2@UiO-66 (1:1, 1:2, 1:3).

Electrochemical Impedance Spectroscopy (EIS) is yet another parameter which is important for the understanding of the kinetic mode of the prepared catalyst. The frequency range used for EIS was 200 kHz–0.1 Hz. Figure 10(a) demonstrates a Nyquist plot with actual impedance on the x-axis as well as fictitious impedance on the y-axis. The Nyquist plot which has a simple Randles circuit gives information on charge transfer resistance (Rct), Solution resistance (Rs), and faradaic capacitance at the electrode/electrolyte interface (Cf). Table-4 shows the comparative values. Small charge transfer resistance (Rct) values, in general, are associated with rapid charge transfer kinetics[2, 115].

In comparison, WS_2@UiO-66(1:2) exhibits interface between catalyst and electrolyte with the lowest charge transfer resistance. Rapid kinetics are proposed by the tiny R_{ct} of WS_2@UiO-66(1:2), which corresponds with Tafel slope attributes and LSV results. Electrochemical Active surface area is an excellent method for determining catalyst activity (ECSA). Electrocatalysts with higher ECSAs require lower reaction

overpotentials. ECSA is calculated by determining the double-layer capacitance (Cdl) using Equation (4).

$$ECSA = C_{dl}/C_f \qquad (4)$$

$$C_{dl} = \frac{(Y_O^{*} R_P)^{1/\alpha}}{Rp} \qquad (5)$$

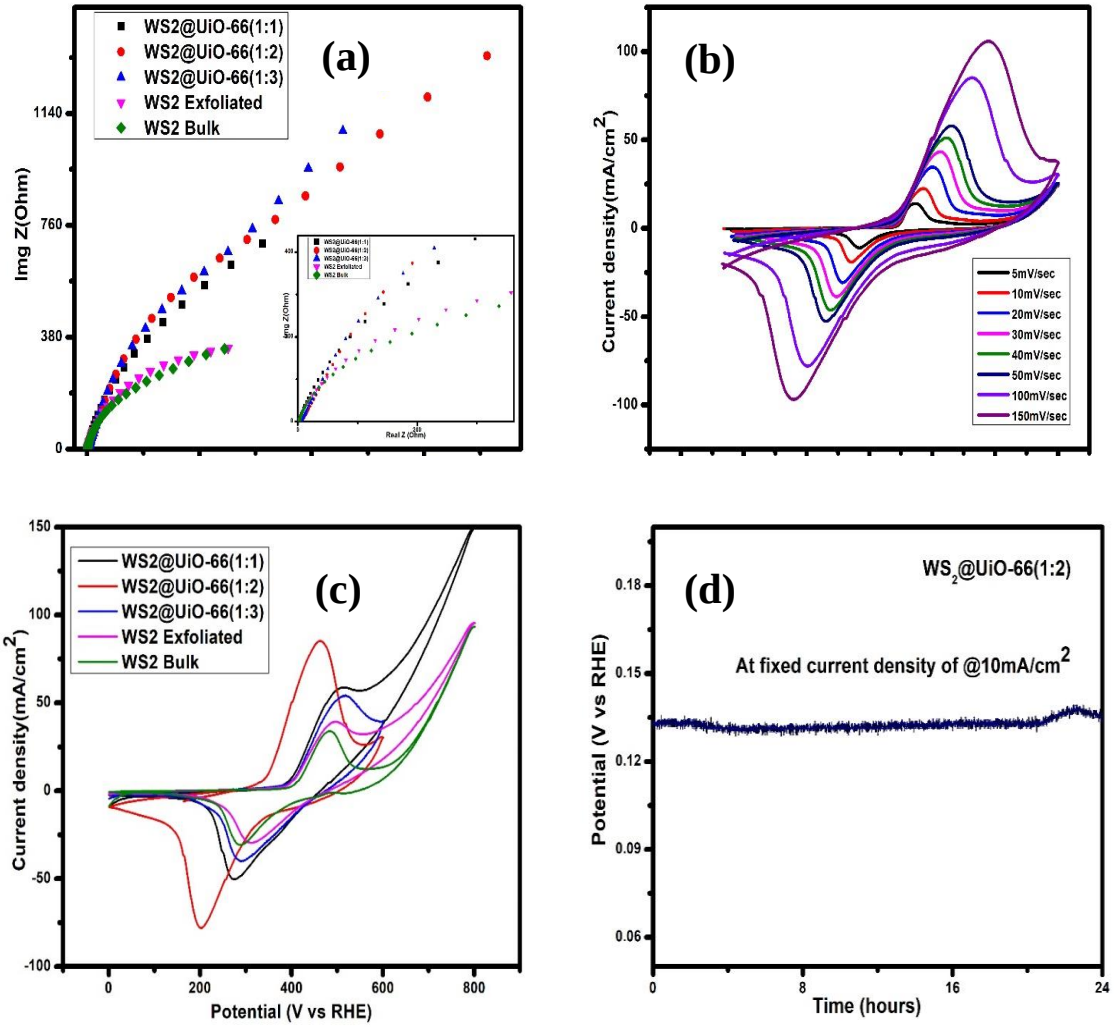

Figure 10 (a) Electrochemical Impedance Spectroscopy (EIS), Nyquist plots of all prepared hybrids (b) CV of WS2@UiO-66 (1:2) at different scan rate (c) CV of all prepared hybrids at scan rate of 50mV/S (d) Stability test at fixed current density of 10mA/cm^2

Electrocatalyst	R_{ct} (ohms)	R_s(ohms)	ECSA ($cm^{2)}$
WS_2@UiO-66(1:1)	5.4	9.3	831.71
WS_2@UiO-66(1:2)	2.65	4.7	1068
WS_2@UiO-66(1:3)	4.6	5.9	586
Bulk WS_2	11	45	400
Exfoliated WS_2	9.8	42	542

To check the cyclic stability of the prepare hybrid, cyclic voltammetry of WS_2@UiO-66 (1:2) was done at various scan rates. Figure 10(b) demonstrates a steady increase in exchange current density when voltage is increased, indicating cyclic stability, strong electrocatalyst efficiency, and low resistance of prepare catalysts, as well as a considerable drop in charge transfer resistance as potential is increased. Cyclic voltammetry (CV) of Bulk WS_2, Exfoliated WS_2, and WS_2@UiO-66 (1:1, 1:2, 1:3) were carried out at 100 mV/s scan rate in 1.0 M KOH electrolyte solution to identify the correlation among current density and voltage over a range (Figure. 6(c)). CV graphs provide information on redox reaction thermodynamics and the electron-transfer reaction kinetic model. The CV curves clearly reveal two well-defined redox peaks. In comparison, WS_2@UiO-66 (1:2) has a larger current density, implying lower diffusion layer resistance and cyclic stability. The charge that travels through the cell is equivalent to the current density.

Furthermore, the catalyst's durability is crucial for commercializing the hydrogen production as a fuel concept. Figure-10(d) shows the stability of WS2@UiO-66 (1:2) after 24 hours of testing. The potential response was found to remain consistent after the WS_2@UiO-66 (1:2) catalyst was activated, with no significant reduction in activity.

Table 5 Comparisons of electrocatalyst HER and OER activity with previously reported catalysts.

Electrocatalysts	**Current density (mA/cm^2)**	**Overpotential HER (mV)**	**Overpotential OER (mV)**	**Stability (hours)**	**Ref.**
WS2@UiO-66(1:2)	10	121	220	24	This work
Mo2S/ UiO-66	10	129.4	180	24	[7]
CoO_x/ UiO-66-300	10	-	283	10	[116]
$WS_2@Co_3S_4$ NW/CC	10	82	280	24	[1]
Ag/ WS_2	10	180	-	24	[117]
WS_2-Co	10	210	-	24	[61]
Ni/WS	8.6	250		24	[118]
$W_{1-x}S_{2-}$ Mo_x@CFP	10	178	-	18	[119]
$WS_2@Co_{(1-x)}$,S,N	10	220	365	-	[120]

Conclusions

One of the most innovative technologies that is now available is one that generates hydrogen by splitting water into its component parts in order to alleviate worries about the environment and provide a sustainable source of energy. A variety of transition metal Sulfides, nitrides, and carbides are being investigated as water-splitting electrocatalysts. Developing highly catalytically active bifunctional catalysts with low conductivity and charge transfer for OER and HER difficulties is a difficult and time-consuming undertaking. For HER and OER, the researchers are looking at novel catalyst material with larger energy conversion rate and small overpotential. Some of these bifunctional heterostructures are demonstrated to exhibit increased performance of OER and HER processes, resulting in the production of hydrogen fuel. This work demonstrates the one-pot solvothermal method used to produce the 2D bifunctional Tungsten disulfide embedded with UiO-66 (WS_2@UiO-66) hybrids and their structure affects its properties and performance of water splitting. The results also showed that by using different reactions and different reactants conditions for hybrid production results in varied interactions between WS_2 and UiO-66. As a result, the morphological geometry, and electro catalytic characteristics of the catalysts are affected. WS_2@UiO-66 (1:2) demonstrated exceptional electro catalytic activity, achieving a current density of 10 mA/cm^2 with HER overpotentials of 121 mV and OER overpotentials of 220 mV. The WS_2@UiO-66 (1:2) maintain their stability after 24 hours so this electrocatalyst very suitable for commercialization. Increased surface area, metal synergistic effects, and excellent electron transport route adjustment, the MOF network's presence of conductive pathways all contribute to enhanced performance. These discoveries lay the foundation for bi-functional hybrids electro catalysts design and production in water-splitting devices. To develop better catalysts understanding, a deeper understanding at the molecular level of process kinetics, the electron transfer mechanism and electro catalysts structural information is required.

Future Recommendations

Despite a significant amount of research and a number of significant advances, it will be quite some time before the technology that splits water into hydrogen and oxygen can be put to practical use. Future catalyst development efforts should focus on a number of main goals, include improving the water-splitting process more ecologically and economically viable. (i) In depth mechanistic investigations of catalysts at the atomic level are still lacking. An in-depth look of the catalytic mechanism might point you in the right route for improving the materials' capabilities. The process's kinetics and catalytic mechanisms may be thoroughly investigated combining theoretical modelling and in-situ characterization techniques. (ii) Catalyst performance can't be easily compared due to the use of a variety of calculation method, such as different substrates for catalysts varied electrode preparation processes, different catalyst mass loadings, different operating conditions, etc. The establishment of standardized testing is critical for comparing different materials studied at various points and times. To properly communicate the results, the use of standard techniques under equal standard circumstances to make objective comparisons of electrocatalyst activity is recommended. (iii) Despite the fact that water-splitting is a hot issue of research. In conditions of new catalyst materials with advantageous design structures, properties, and active sites, there are still a few areas that need to be investigated. (iv)A catalyst's charge transfer characteristics have not been thoroughly examined.

References:

[1]. Zhang, T., et al., Bifunctional WS2@ Co3S4 core-shell nanowire arrays for efficient water splitting. 2022. **404**: p. 139648.

[2]. Abdullah, U., M. Ali, and E. Pervaiz, An Inclusive Review on Recent Advancements of Cadmium Sulfide Nanostructures and its Hybrids for Photocatalytic and Electrocatalytic Applications. Molecular Catalysis, 2021. **508**: p. 111575.

[3]. Kumar, R., et al., Strong interactions between the nanointerfaces of silica-supported Mo2C/MoP heterojunction promote hydrogen evolution reaction. 2020. **12**(52): p. 57898-57906.

[4]. Pu, Z., et al., Single-atom catalysts for electrochemical hydrogen evolution reaction: recent advances and future perspectives. 2020. **12**(1): p. 1-29.

[5]. Abdullah, U., M. Ali, and E.J.I.J.o.H.E. Pervaiz, Cadmium sulfide embedded Prussian Blue as highly active bifunctional electrocatalyst for water-splitting process. 2022.

[6]. Hosseini, H. and M.J.C.E.J. Roushani, Rational design of hollow core-double shells hybrid nanoboxes and nanopipes composed of hierarchical Cu-Ni-Co selenides anchored on nitrogen-doped carbon skeletons as efficient and stable bifunctional electrocatalysts for overall water splitting. 2020. **402**: p. 126174.

[7]. Ali, M. and E.J.M.C. Pervaiz, Effect of synthesis route on electrocatalytic water-splitting activity of MoS2/UiO-66 hybrid. 2022. **519**: p. 112136.

[8]. Hei, J., et al., NiFeP nanosheets on N-doped carbon sponge as a hierarchically structured bifunctional electrocatalyst for efficient overall water splitting. 2021. **549**: p. 149297.

[9]. Zeleke, T.S., et al., Immobilized single molecular molybdenum disulfide on carbonized polyacrylonitrile for hydrogen evolution reaction. 2019. **13**(6): p. 6720-6729.

[10]. Ali, M., E. Pervaiz, and O.J.A.o. Rabi, Enhancing the Overall Electrocatalytic Water-Splitting Efficiency of Mo2C Nanoparticles by Forming Hybrids with UiO-66 MOF. 2021. **6**(50): p. 34219-34228.

[11]. Rabi, O., et al., Bifunctional Molybdenum Carbide based Hybrids for Electrocatalytic Water splitting. Ceramics International, 2021.

[12]. Zahra, R., et al., A review on nickel cobalt sulphide and their hybrids: Earth abundant, pH stable electro-catalyst for hydrogen evolution reaction. International Journal of Hydrogen Energy, 2020.

[13]. Abdullah, U., et al., An inclusive perspective on the recent development of tungsten-based catalysts for overall water-splitting: A review. 2022.

[14]. Feng, Z., et al., Controllable synthesis of flower-like Mn-Co-P nanosheets as bifunctional electrocatalysts for overall water splitting. 2021. **615**: p. 126265.

[15]. Paudel, D.R., et al., Fe and P doped 1T-phase enriched WS23D-dendritic nanostructures for efficient overall water splitting. 2021. **286**: p. 119897.

[16]. Kou, T., S. Wang, and Y.J.A.M.L. Li, Perspective on high-rate alkaline water splitting. 2021. **3**(2): p. 224-234.

[17]. Zhou, B., et al., Engineering P-doped Ni3S2-NiS hybrid nanorod arrays for efficient overall water electrolysis. 2021. **862**: p. 158391.

[18]. Khan, R., et al., 3D hierarchical heterostructured LSTN@ NiMn-layered double hydroxide as a bifunctional water splitting electrocatalyst for hydrogen production. 2021. **285**: p. 119174.

[19]. Zhang, H., et al., Bifunctional heterostructured transition metal phosphides for efficient electrochemical water splitting. 2020. **30**(34): p. 2003261.

[20]. Zhang, R., et al., Dual synergistic effect of S-doped carbon bridged semi crystalline MILN-based Co3S4/MnS2 nanostructure in electrocatalytic overall water splitting. 2021. **366**: p. 137438.

[21]. Li, Y., et al., Heterostructured MoO2@ MoS2@ Co9S8 nanorods as high efficiency bifunctional electrocatalyst for overall water splitting. 2021. **543**: p. 148804.

[22]. Liu, Y., et al., Hierarchically heterostructured metal hydr (oxy) oxides for efficient overall water splitting. 2019. **11**(24): p. 11736-11743.

[23]. Vikraman, D., et al., Improved Hydrogen Evolution Reaction Performance using MoS2–WS2 Heterostructures by Physicochemical Process. ACS Sustainable Chemistry & Engineering, 2018. **6**(7): p. 8400-8409.

[24]. Yin, W., et al., Low-temperature one-pot synthesis of WS2 nanoflakes as electrocatalyst for hydrogen evolution reaction. 2018. **30**(4): p. 045603.

[25]. Sun, C., et al., N-doped WS 2 nanosheets: a high-performance electrocatalyst for the hydrogen evolution reaction. 2016. **4**(29): p. 11234-11238.

[26]. Pesci, F.M., et al., MoS2/WS2 heterojunction for photoelectrochemical water oxidation. 2017. **7**(8): p. 4990-4998.

[27]. Voiry, D., et al., Enhanced catalytic activity in strained chemically exfoliated WS2 nanosheets for hydrogen evolution. 2013. **12**(9): p. 850-855.

[28]. Wang, J., et al., Recent progress in cobalt-based heterogeneous catalysts for electrochemical water splitting. 2016. **28**(2): p. 215-230.

[29]. You, B. and Y.J.A.o.c.r. Sun, Innovative strategies for electrocatalytic water splitting. 2018. **51**(7): p. 1571-1580.

[30]. Li, W., C. Wang, and X.J.J.o.M.C.A. Lu, Integrated transition metal and compounds with carbon nanomaterials for electrochemical water splitting. 2021. **9**(7): p. 3786-3827.

[31]. Zou, X. and Y.J.C.S.R. Zhang, Noble metal-free hydrogen evolution catalysts for water splitting. 2015. **44**(15): p. 5148-5180.

[32]. Morales-Guio, C.G., L.-A. Stern, and X.J.C.S.R. Hu, Nanostructured hydrotreating catalysts for electrochemical hydrogen evolution. 2014. **43**(18): p. 6555-6569.

[33]. Lan, Z.-A., G. Zhang, and X.J.A.C.B.E. Wang, A facile synthesis of Br-modified g-C3N4 semiconductors for photoredox water splitting. 2016. **192**: p. 116-125.

[34]. Busch, M., et al., Beyond the top of the volcano?–A unified approach to electrocatalytic oxygen reduction and oxygen evolution. 2016. **29**: p. 126-135.

[35]. Suen, N.-T., et al., Electrocatalysis for the oxygen evolution reaction: recent development and future perspectives. 2017. **46**(2): p. 337-365.

[36]. Wang, X., et al., Electronic and structural engineering of carbon-based metal-free electrocatalysts for water splitting. 2019. **31**(13): p. 1803625.

[37]. Vishwakarma, A.K., et al., Band gap engineering of Gd and Co doped BiFeO3 and their application in hydrogen production through photoelectrochemical route. 2017. **42**(36): p. 22677-22686.

[38]. Lin, H.-W., et al., Bi-metallic MOFs possessing hierarchical synergistic effects as high performance electrocatalysts for overall water splitting at high current densities. 2019. **258**: p. 118023.

[39]. Amano, F., E. Ishinaga, and A.J.T.J.o.P.C.C. Yamakata, Effect of particle size on the photocatalytic activity of WO3 particles for water oxidation. 2013. **117**(44): p. 22584-22590.

[40]. Almquist, C.B. and P.J.J.o.C. Biswas, Role of synthesis method and particle size of nanostructured TiO2 on its photoactivity. 2002. **212**(2): p. 145-156.

[41]. Anantharaj, S. and V.J.A.E.M. Aravindan, Developments and Perspectives in 3d Transition-Metal-Based Electrocatalysts for Neutral and Near-Neutral Water Electrolysis. 2020. **10**(1): p. 1902666.

[42]. Kear, G., F.C.J.C. Walsh, and materials, The characteristics of a true Tafel slope. 2005. **30**(6): p. 51-55.

[43]. Lu, J., S. Yin, and P.K.J.E.E.R. Shen, Carbon-encapsulated electrocatalysts for the hydrogen evolution reaction. 2019. **2**(1): p. 105-127.

[44]. Anantharaj, S., et al., Recent trends and perspectives in electrochemical water splitting with an emphasis on sulfide, selenide, and phosphide catalysts of Fe, Co, and Ni: a review. 2016. **6**(12): p. 8069-8097.

[45]. Wang, J., et al., Earth-abundant transition-metal-based bifunctional catalysts for overall electrochemical water splitting: A review. 2020. **819**: p. 153346.

[46]. Liu, K., et al., Recent advances in metal–nitrogen–carbon catalysts for electrochemical water splitting. 2017. **1**(11): p. 2155-2173.

[47]. Anantharaj, S., et al., Precision and correctness in the evaluation of electrocatalytic water splitting: revisiting activity parameters with a critical assessment. 2018. **11**(4): p. 744-771.

[48]. Shi, Y. and B.J.C.S.R. Zhang, Recent advances in transition metal phosphide nanomaterials: synthesis and applications in hydrogen evolution reaction. 2016. **45**(6): p. 1529-1541.

[49]. Ye, L., et al., Fabrication and enhanced photoelectrochemical performance of MoS2/S-doped g-C3N4 heterojunction film. 2016. **8**(8): p. 5280-5289.

[50]. Cheng, L., et al., Ultrathin WS2 nanoflakes as a high-performance electrocatalyst for the hydrogen evolution reaction. 2014. **126**(30): p. 7994-7997.

[51]. Voiry, D., et al., Enhanced catalytic activity in strained chemically exfoliated WS 2 nanosheets for hydrogen evolution. 2013. **12**(9): p. 850-855.

[52]. Zhu, H., et al., When cubic cobalt sulfide meets layered molybdenum disulfide: a core–shell system toward synergetic electrocatalytic water splitting. 2015. **27**(32): p. 4752-4759.

[53]. Zhang, J., et al., Interface engineering of MoS2/Ni3S2 heterostructures for highly enhanced electrochemical overall-water-splitting activity. 2016. **128**(23): p. 6814-6819.

[54]. Wang, D., et al., When NiO@ Ni meets WS2 nanosheet array: a highly efficient and ultrastable electrocatalyst for overall water splitting. 2018. **4**(1): p. 112-119.

[55]. Peng, S., et al., Engineering Co 9 S 8/WS 2 array films as bifunctional electrocatalysts for efficient water splitting. 2017. **5**(44): p. 23361-23368.

[56]. Liu, S., et al., Ultrathin WS2 nanosheets vertically aligned on TiO2 nanobelts as efficient alkaline hydrogen evolution electrocatalyst. 2020. **45**(3): p. 1697-1705.

[57]. Tayebi, M., Z. Masoumi, and B.-K.J.U.s. Lee, Ultrasonically prepared photocatalyst of W/WO3 nanoplates with WS2 nanosheets as 2D material for improving photoelectrochemical water splitting. 2021. **70**: p. 105339.

[58]. Velpandian, M., et al., Improved charge carrier dynamics of WS 2 nanostructures by the way of CdS@ WS 2 heterostructures for use in water splitting and water purification. 2020. **4**(8): p. 4096-4107.

[59]. Ryu, H., et al., Ferroelectric tunneling junctions based on aluminum oxide/zirconium-doped hafnium oxide for neuromorphic computing. 2019. **9**(1): p. 1-8.

[60]. Xu, R., et al., Cobalt-Doped Tungsten Sulfides as Stable and Efficient Air Electrodes for Rechargeable Zinc-Air Batteries. 2020. **7**(1): p. 148-154.

[61]. Shi, X., et al., Rapid flame doping of Co to WS 2 for efficient hydrogen evolution. 2018. **11**(8): p. 2270-2277.

[62]. Yang, L., et al., Amorphous nickel/cobalt tungsten sulfide electrocatalysts for high-efficiency hydrogen evolution reaction. 2015. **341**: p. 149-156.

[63]. Tran, P.D., et al., Novel cobalt/nickel–tungsten-sulfide catalysts for electrocatalytic hydrogen generation from water. 2013. **6**(8): p. 2452-2459.

[64]. Jiang, A., et al., Vanadium-Doped WS2 Nanosheets Grown on Carbon Cloth as a Highly Efficient Electrocatalyst for the Hydrogen Evolution Reaction. 2018. **13**(11): p. 1438-1446.

[65]. Chua, X.J., et al., Negative electrocatalytic effects of p-doping niobium and tantalum on MoS2 and WS2 for the hydrogen evolution reaction and oxygen reduction reaction. 2016. **6**(9): p. 5724-5734.

[66]. Yang, Q., et al., Composite electrocatalyst Mo x W 1-x S 2 nanosheets on carbon fiber paper for highly efficient hydrogen evolution reaction. 2018. **22**(10): p. 2969-2976.

[67]. Shifa, T.A., et al., Engineering the Electronic Structure of 2D WS2 Nanosheets Using Co Incorporation as CoxW (1-x) S2 for Conspicuously Enhanced Hydrogen Generation. 2016. **12**(28): p. 3802-3809.

[68]. Liu, Z., et al., Colloidal synthesis of 1T'phase dominated WS2 towards endurable electrocatalysis. 2018. **50**: p. 176-181.

[69]. Maiti, A. and S.K.J.J.o.M.C.A. Srivastava, Sulphur edge and vacancy assisted nitrogen–phosphorus co-doped exfoliated tungsten disulfide: a superior electrocatalyst for hydrogen evolution reaction. 2018. **6**(40): p. 19712-19726.

[70]. Hussain, S., et al., Synthesis of MoS 2 (1− x) Se 2x and WS 2 (1− x) Se 2x alloys for enhanced hydrogen evolution reaction performance. 2017. **4**(12): p. 2068-2074.

[71]. Zhang, Y., et al., Dendritic growth of monolayer ternary WS 2 (1− x) Se 2x flakes for enhanced hydrogen evolution reaction. 2017. **9**(17): p. 5641-5647.

[72]. Sarma, P.V., et al., Oxygen incorporated WS 2 nanoclusters with superior electrocatalytic properties for hydrogen evolution reaction. 2018. **10**(20): p. 9516-9524.

[73]. Shifa, T.A., et al., Efficient catalysis of hydrogen evolution reaction from WS2 (1− x) P2x nanoribbons. 2017. **13**(16): p. 1603706.

[74]. Zhou, H., et al., Highly efficient hydrogen evolution from edge-oriented WS2 (1–x) Se2 x particles on three-dimensional porous NiSe2 foam. 2016. **16**(12): p. 7604-7609.

[75]. Xu, K., et al., Component-controllable WS2 (1–x) Se2 x nanotubes for efficient hydrogen evolution reaction. 2014. **8**(8): p. 8468-8476.

[76]. Huang, Z., et al., Polyoxometallates@ zeolitic-imidazolate-framework derived bimetallic tungsten-cobalt sulfide/porous carbon nanocomposites as efficient bifunctional electrocatalysts for hydrogen and oxygen evolution. 2020. **330**: p. 135335.

[77]. Fu, Q., et al., Synthesis and enhanced electrochemical catalytic performance of monolayer WS2 (1–x) Se2x with a tunable band gap. 2015. **27**(32): p. 4732-4738.

[78]. Wang, F., et al., Hydrothermal synthesis of flower-like molybdenum disulfide microspheres and their application in electrochemical supercapacitors. 2018. **8**(68): p. 38945-38954.

[79]. Li, J., et al., A flexible plasma-treated silver-nanowire electrode for organic light-emitting devices. 2017. **7**(1): p. 1-9.

[80]. Nikam, R.D., et al., Three-Dimensional Heterostructures of MoS2 Nanosheets on Conducting MoO2 as an Efficient Electrocatalyst To Enhance Hydrogen Evolution Reaction. ACS Appl Mater Interfaces, 2015. **7**(41): p. 23328-35.

[81]. Ni, Z., et al., Recent Advances in Layered Tungsten Disulfide as Electrocatalyst for Water Splitting. ChemCatChem, 2020. **12**(20): p. 4962-4999.

[82]. Wang, F.-f., et al., WxCoyS core-shell grown on hollow-porous carbon fiber (HCF) as synergetic electrocatalysts for efficient water splitting. Electrochimica Acta, 2019. **306**: p. 437-445.

[83]. Kagkoura, A., et al., Sulfur-doped graphene/transition metal dichalcogenide heterostructured hybrids with electrocatalytic activity toward the hydrogen evolution reaction. Nanoscale Adv, 2019. **1**(4): p. 1489-1496.

[84]. Li, J., et al., Seamless tungsten disulfide-tungsten heterojunction with abundant exposed active sites for efficient hydrogen evolution. Applied Catalysis B: Environmental, 2019. **244**: p. 320-326.

[85]. Ensafi, A.A., et al., WS 2 grafted on silicon and nano-silicon particles etched: a high-performance electrocatalyst for hydrogen evolution reaction. 2018. **15(**3): p. 613-620.

[86]. Chen, N., et al., Three-Dimensional Nanoporous Tungsten Disulfide/Acetylene Black Nanoflower Composite as Efficient Electrocatalyst for Enhanced Hydrogen Evolution Reaction. J Nanosci Nanotechnol, 2019. **19(**2): p. 819-825.

[87]. Tiwari, A.P., et al., Bifunctional oxygen electrocatalysis through chemical bonding of transition metal chalcogenides on conductive carbons. 2017. **7**(14): p. 1602217.

[88]. Zhang, X., et al., Ultrathin WS 2 nanosheets vertically embedded in a hollow mesoporous carbon framework–a triple-shell structure with enhanced lithium storage and electrocatalytic properties. 2018. **6**(39): p. 19004-19012.

[89]. Seo, B., et al., Preferential horizontal growth of tungsten sulfide on carbon and insight into active sulfur sites for the hydrogen evolution reaction. 2018. **10(**8): p. 3838-3848.

[90]. Yao, Y., et al., Graphdiyne-WS2 2D-Nanohybrid electrocatalysts for high-performance hydrogen evolution reaction. 2018. **129**: p. 228-235.

[91]. Li, H., et al., Free-standing N-enriched C foam@ WS2 nanoflakes for efficient electrocatalytic hydrogen evolution. 2019. **487**: p. 972-980.

[92]. Wang, H., et al., Recent advancements in heterostructured interface engineering for hydrogen evolution reaction electrocatalysis. 2020. **8**(15): p. 6926-6956.

[93]. Hussain, S., et al., WS2/CoSe2 heterostructure: A designed structure as catalysts for enhanced hydrogen evolution performance. 2018. **65**: p. 167-174.

[94]. Jing, Y., et al., Enhanced hydrogen evolution reaction of WS2–CoS2 heterostructure by synergistic effect. 2019. **44(**2): p. 809-818.

[95]. Jiang, X., et al., Selective growth of vertically aligned two-dimensional MoS2/WS2 nanosheets with decoration of Bi2S3 nanorods by microwave-

assisted hydrothermal synthesis: Enhanced photo-and electrochemical performance for hydrogen evolution reaction. 2018. **43**(46): p. 21290-21298.

[96]. Zhong, Y., et al., A photo-responsive electrocatalyst: CdSe quantum dot sensitized WS 2 nanosheets for hydrogen evolution in neutral solution. 2018. **42**(22): p. 18021-18027.

[97]. Xiao, P., et al., Fullerene-like WS2 supported Pd catalyst for hydrogen evolution reaction. 2019. **380**: p. 215-223.

[98]. Vikraman, D., et al., Improved hydrogen evolution reaction performance using MoS2–WS2 heterostructures by physicochemical process. 2018. **6**(7): p. 8400-8409.

[99]. Lu, S.-S., et al., Heterostructured binary Ni-W sulfides nanosheets as pH-universal electrocatalyst for hydrogen evolution. 2018. **445**: p. 445-453.

[100]. Zhou, X., et al., Symmetric synergy of hybrid CoS 2–WS 2 electrocatalysts for the hydrogen evolution reaction. 2017. **5**(30): p. 15552-15558.

[101]. Chen, Y., et al., Superior electrocatalysis for hydrogen evolution with crumpled graphene/tungsten disulfide/tungsten trioxide ternary nanohybrids. 2018. **47**: p. 66-73.

[102]. Zhu, Z., et al., Ultrathin transition metal dichalcogenide/3d metal hydroxide hybridized nanosheets to enhance hydrogen evolution activity. 2018. **30**(28): p. 1801171.

[103]. Guo, Z., et al., Large surface and pore structure of mesoporous WS2 and RGO nanosheets with small amount of Pt as a highly efficient electrocatalyst for hydrogen evolution. 2018. **43**(51): p. 22905-22916.

[104]. Hasani, A., et al., The role of metal dopants in WS2 nanoflowers in enhancing the hydrogen evolution reaction. 2018. **567**: p. 73-79.

[105]. Zhang, Y., et al., 2D WS2 nanosheet supported Pt nanoparticles for enhanced hydrogen evolution reaction. 2017. **42**(8): p. 5472-5477.

[106]. Tang, K., et al., High Edge Selectivity of In Situ Electrochemical Pt Deposition on Edge-Rich Layered WS2 Nanosheets. 2018. **30**(7): p. 1704779.

[107]. Jin, J., et al., CoP nanoparticles combined with WS2 nanosheets as efficient electrocatalytic hydrogen evolution reaction catalyst. 2017. **42**(7): p. 3947-3954.

[108]. Liu, Y., et al., The highly enhanced performance of lamellar WS 2 nanosheet electrodes upon intercalation of single-walled carbon nanotubes for supercapacitors and lithium ions batteries. 2014. **50**(34): p. 4485-4488.

[109]. Zhang, X.-F., et al., Adsorptive desulfurization from the model fuels by functionalized UiO-66 (Zr). 2018. **234**: p. 256-262.

[110]. Bushroa, A.R., et al., Approximation of crystallite size and microstrain via XRD line broadening analysis in TiSiN thin films. 2012. **86**(8): p. 1107-1112.

[111]. Schaate, A., et al., Modulated synthesis of Zr-based metal–organic frameworks: from nano to single crystals. 2011. **17**(24): p. 6643-6651.

[112]. Chen, H., et al., Silver nanoparticles on UiO-66 (Zr) metal-organic frameworks for water disinfection application. 2022. **11**(2): p. 269-276.

[113]. Swathi, S., et al., Surfactant-assisted tungsten sulfide mesoporous sphere for hydrogen production. 2021.

[114]. Ehsan, M.A., A.S. Hakeem, and A.J.S.r. Rehman, Synergistic effects in bimetallic Pd–CoO electrocatalytic thin films for oxygen evolution reaction. 2020. **10**(1): p. 1-11.

[115]. Hu, X., et al., Nickel foam and stainless steel mesh as electrocatalysts for hydrogen evolution reaction, oxygen evolution reaction and overall water splitting in alkaline media. 2019. **9**(54): p. 31563-31571.

[116]. Charles, V., et al., CoO x/UiO-66 and NiO/UiO-66 heterostructures with UiO-66 frameworks for enhanced oxygen evolution reactions. 2021. **45**(32): p. 14822-14830.

[117]. Pataniya, P.M. and C.J.A.S.S. Sumesh, Enhanced electrocatalytic hydrogen evolution reaction by injection of photogenerated electrons in Ag/WS2 nanohybrids. 2021. **563**: p. 150323.

[118]. Yang, L., et al., Amorphous nickel/cobalt tungsten sulfide electrocatalysts for high-efficiency hydrogen evolution reaction. Applied Surface Science, 2015. **341**: p. 149-156.

[119]. Yang, Q., et al., Composite electrocatalyst MoxW1-xS2 nanosheets on carbon fiber paper for highly efficient hydrogen evolution reaction. 2018. **22**(10): p. 2969-2976.

[120]. Huang, Z., et al., Polyoxometallates@zeolitic-imidazolate-framework derived bimetallic tungsten-cobalt sulfide/porous carbon nanocomposites as efficient bifunctional electrocatalysts for hydrogen and oxygen evolution. Electrochimica Acta, 2020. **330**: p. 135335.